The 2022 WMO Technical Conference on Meteorological and Environmental Instruments and Methods of Observation (TECO-2022)

10-13 October 2022, Paris (France)

Computational Fluid Dynamics and wind tunnel investigation of the aerodynamic response of the Thies LPM©

Enrico Chinchella[1,2]; Arianna Cauteruccio[1,2]; Luca G. Lanza[1,2]

[1] University of Genova, Dep. of Civil, Chemical and Environmental Engineering (DICCA), Genoa, Italy

[2] WMO/CIMO Lead Centre "B. Castelli" on Precipitation Intensity, Italy

Corresponding author: Enrico Chinchella, enrico.chinchella@edu.unige.it

Abstract:

Optical disdrometers are being increasingly adopted by meteorological services for precipitation measurements due to their capability to provide additional information than the precipitation rate alone. They identify hydrometeors by coupling particle size and fall velocity. The Thies Laser Precipitation Monitor (LPM) uses an optical sensor to detect the obstruction of an infrared laser beam caused by the crossing hydrometeors. However, measurements can be affected by wind and by the airflow deformation produced by the bluff-body aerodynamic behaviour of the instrument. The airflow field around the instrument geometry is numerically simulated in this work using Computational Fluid Dynamics (CFD). Simulations were performed by means of the OpenFOAM software, solving the Navier-Stokes equations under the URANS (Unsteady Reynolds Averaged Navier-Stokes) approximation and the Shear Stress Transport – SST k-ω turbulence model. Different wind velocity conditions were simulated and, due to the complex, non-axisymmetric geometry, different orientations of the instrument with respect to the incoming wind were also simulated. Simulation results were validated through local flow velocity measurements obtained in the DICCA wind tunnel. The Thies LPM was mounted in the wind tunnel chamber on to a rotating plate and the airflow velocity was sampled at multiple positions around the instrument. The measurements were obtained using a traversing system equipped with a "Cobra" multi-hole pressure probe, which provides the three velocity components of the local flow. Results show that the numerical simulation setup is suitable to provide an accurate description of the flow field around the gauge and inside the measurement area of the gauge. These results will be used to identify the less impacting wind direction and possible correction in case of measurements taken in windy conditions.

1. Introduction

Currently, non-catching type gauges (hereinafter NCGs) are being developed and increasingly adopted by national weather services (NWS). These gauges measure precipitation by sensing each hydrometeor independently, with no need to collect water in a container. NCGs are often capable of sensing both the hydrometeors size and fall velocity, depending on the measurement principle exploited. Due to the sensor used they usually present a complex, often non-axisymmetric outer design. NCGs have several advantages over traditional catching gauges (CGs) like the ability to provide several precipitation parameters at a high temporal resolution. Furthermore, they require less maintenance and are well suited for automatic weather stations, fostering their incremental adoption.

The most relevant factors still preventing a widespread diffusion of NCGs are the lack of standardised calibration procedures and correction algorithms to compensate for instrumental and environmental biases [1]. Amongst the latter, wind is the primary source of bias [2], due to the gauge body itself that, immersed in a wind field, behaves like a bluff-body obstacle to the undisturbed airflow, producing strong velocity gradients, vertical components, and the development of turbulence close to the gauge surface (see, e.g., [3,4]). Trajectories of the incoming hydrometeors are diverted due to this effect, depending on their diameter, the gauge shape, wind speed, and wind direction, leading to an over or under estimation of the precipitation amount and intensity (see, e.g., [5]). This effect, well documented in the literature for CGs, is amplified in the case of NCGs due to their measurement principles and non-axisymmetric shape that implies a dependency of the aerodynamic effect on the wind direction.

To quantify the effect of wind on the instruments, field campaigns, wind tunnel (WT) testing and numerical simulation can be employed. The latter is in general preferred, due to lower costs and the ability to easily test different configurations (see e.g., [4,6]). In this work, numerical simulation of the wind-induced airflow pattern near the laser precipitation monitor (LPM) were performed. This NCG is widely used by researchers, see, e.g., [7–10], and is being progressively adopted by NWS, thanks to its performance and relatively low cost [11]. Upton and Brawn [12] show that two such instruments, installed orthogonally to each other, may report differences of up to 20% in the total number of detected hydrometeors, even at limited wind speed, suggesting that wind direction has a strong role in the amount of measurement bias in windy conditions for this instrument.

2. Method

The Thies LPM employs an IR laser beam to detect hydrometeors in flight. As shown in Figure 1, the instrument body is composed of a prismatic housing for the circuitry boards, with attached the light emitting head and two supporting arms. Located at the end of the two arms, and aligned with the emitting head, is the receiving sensor. The instrument produces an infrared light sheet (228 mm long and 20 mm wide) with a thickness of 0.75 mm. A photodiode in the receiving head is used to convert the laser beam power into an electric signal. When each single hydrometeor crosses the beam, the receiver will detect a reduction in the electric signal. The diameter of the particle is calculated as a function of the voltage drop, while its fall velocity is obtained from the duration of the voltage reduction.

Figure 1: The Thies LPM, with the emitting head (attached to the circuitry box on the left-hand side) and the receiving head (attached to the supporting arms on the right-hand side).

a. CFD simulation

CFD simulations are used in this work to assess the effect of the Thies LPM instrument body on the wind velocity field, and the numerical results are validated by means of wind tunnel measurements. The OpenFOAM software was used to simulate the airflow pattern near the instrument body, solving the Unsteady Reynolds-Averaged Navier–Stokes (URANS) equations by means of a pseudo-transient approach, based on a local time stepping (LTS) numerical scheme [13]. The computational mesh was produced for a 4 m long, 2.4 m wide, and 2 m high simulation domain with a maximum cell size of 0.04 m that is progressively refined (up to 1 mm near the instrument walls) to reproduce the finer geometrical details and to enhance the modelling of turbulence. To simulate the variable direction of the incoming wind, nine different meshes were realized by rotating the instrument from α = 0° to α = 180° with increments of 22.5° (α is the angle between the wind direction and the main symmetry axis of the instrument). For each wind direction, five wind speed values (U_{ref}) equal to 2, 5, 10, 15, and 20 m/s were tested. Evaluation of the mesh resolution requirements was achieved by computing the ratio between the integral length scale and the grid length scale, named R_l. For URANS simulations a generally accepted criterion is $Rl \geq 5$, so that the larger eddies, adding-up to 80% of the turbulence kinetic energy, are discretized by at least 5 cells [14]. In this work the k-ω shear stress transport (SST) turbulence model is used, where k is the turbulent kinetic energy and ω the specific turbulent dissipation rate, therefore the integral length scale (L_0) is calculated from Equation (1) [15], while R_l is calculated from Equation (2), where the coefficient C_μ is equal to 0.09 and V is the volume of the cell.

$$L_0 = \frac{k^{1/2}}{C_\mu \cdot \omega} \quad (1) \qquad R_l = \frac{L_0}{\sqrt[3]{V}} \quad (2)$$

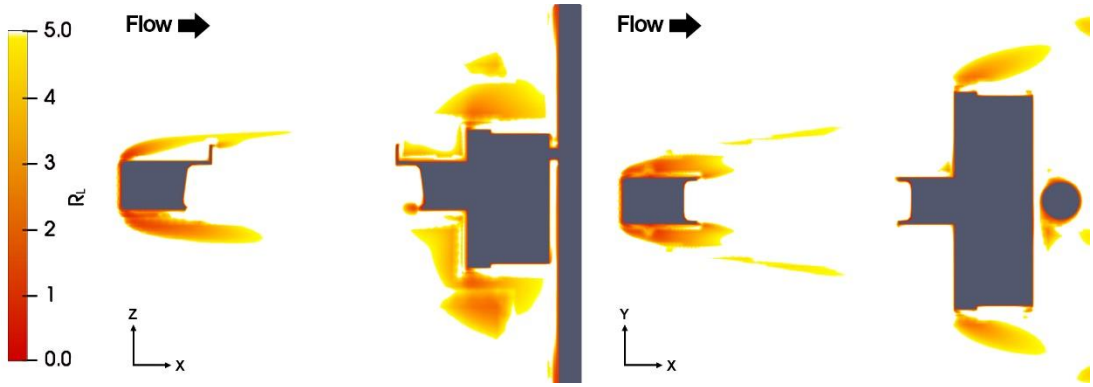

Figure 2: Maps of the RL ratio for a wind speed of 10 m/s and α = 0°.

In Figure 2, maps of the achieved R_l values along two sections of the domain are shown. Only in the proximity of the straight and sharp edges the R_l criterion could not be met. With this approach, the final meshes contain between four and five million cells, an example of which is shown in Figure 3. Finally, simulations were conducted by setting air as an incompressible fluid, with a density of 1.0 kg/m^3 and a kinematic viscosity of 1.5 × 10−5 m^2/s, the free stream turbulence intensity was set equal to 1%.

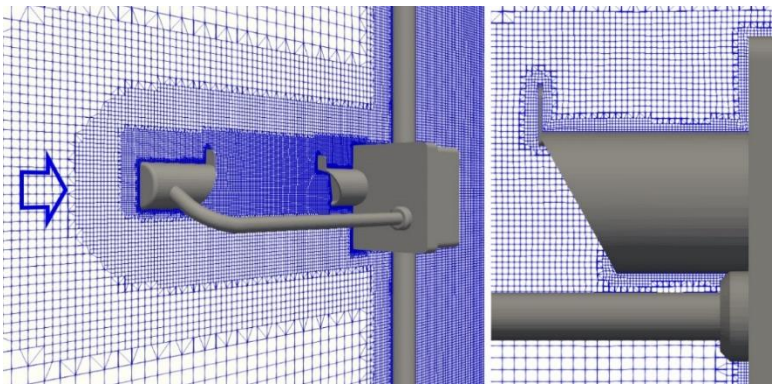

Figure 3: The computational mesh along the longitudinal cross-section of the domain around the Thies LPM for the configuration at α = 0° (left-hand panel). The arrow indicates the direction of the incoming undisturbed wind flow. Close-up details of the mesh near the instrument emitting head (right-hand panel).

b. Wind tunnel measurements

The experimental campaign was conducted in the WT facility available at the Department of Civil, Chemical and Environmental Engineering (DICCA) of the University of Genova. Measurements were taken using a multi-hole pressure probe, called "Cobra" [16], attached to a traversing arm with three-degrees of freedom. A full-scale Thies LPM instrument was installed in the WT, fixed to a rotating baseplate (see Figure 4). For each of the nine wind directions investigated, the baseplate was rotated aligning the instrument to be at the correct angle with the flow. The airflow velocity was set equal to 5 and 10 m/s and for α = 0°, 45°, and 90°, while a reduced number of probe positions were sampled also at U_{ref} = 3, 7.5, and 15 m/s, to investigate the scalability (Reynolds dependency) of the flow field. In total, 915 flow velocity measurements were obtained.

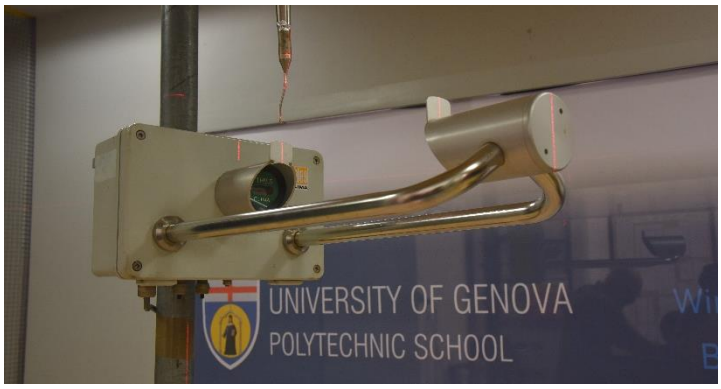

Figure 4: The Thies LPM during the installation procedure in the DICCA WT for the configuration at α = 0°. The instrument and the Cobra probe are aligned by employing a laser beam.

3. Results and discussion

a. CFD simulation results

As a sample of the large numerical dataset obtained from CFD simulations, wind velocity maps are shown along a plane parallel to the instrument main symmetry axis (figure 5, 6 and 7). In the left-hand panels, the red zones indicate a larger flow velocity than the undisturbed wind speed, while in the blue zones the flow velocity is lower. In the right-hand panels, the red zones indicate upward flow velocity components while downward components occur in the blue zones.

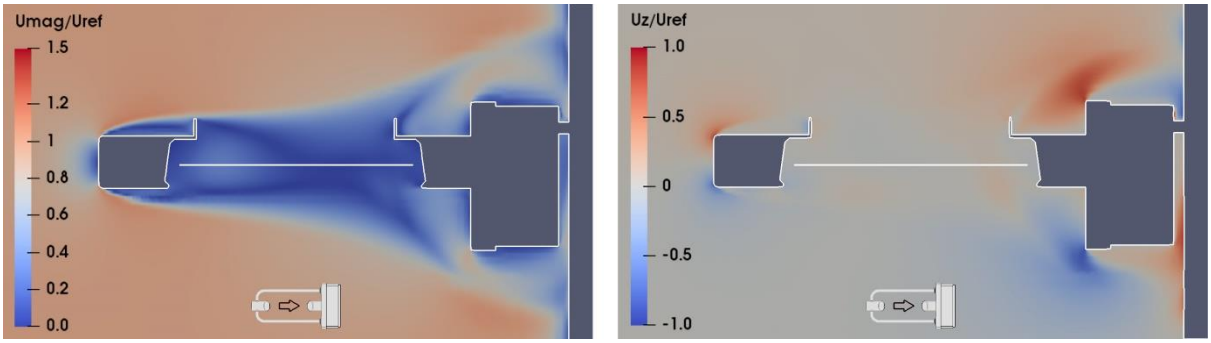

Figure 5: CFD simulation at 10 m/s and α = 0°; maps of the normalized magnitude and vertical component of the flow velocity (left- and right-hand panel, respectively). The white horizontal line indicates the position of the sensing area of the instrument, while the small arrow indicates the undisturbed flow direction.

In Figure 5, at α = 0° and wind speed 10m/s, the receiver head is the first bluff-body obstacle to the flow, which generates accelerated and vertical velocity components above and below the sensing area of the instrument (white horizontal line).

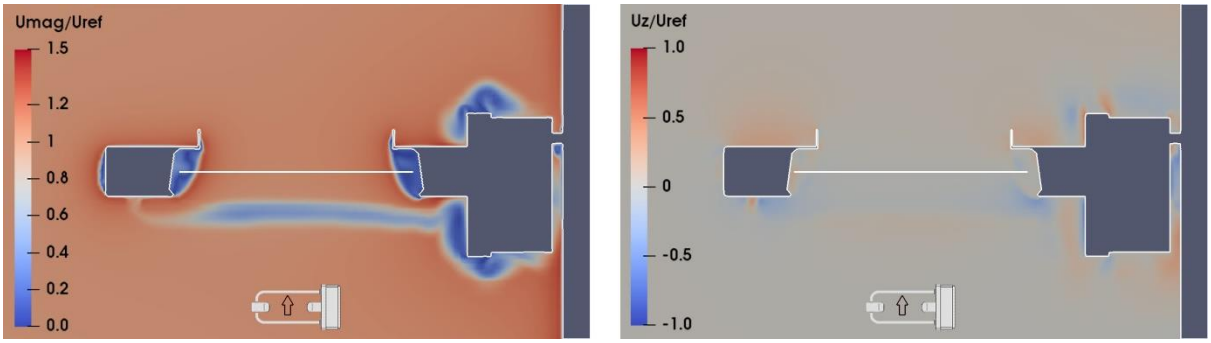

Figure 6: CFD simulation at 10 m/s and α = 90°; maps of the normalized magnitude and vertical component of the flow velocity (left- and right-hand panel, respectively). The white horizontal line indicates the position of the sensing area of the instrument, while the small arrow indicates the undisturbed flow direction.

In Figure 6, at α = 90° and wind speed 10m/s, the flow near the sensing area is mostly undisturbed. The shedding of vortices generated by the supporting arms produces only a limited influence on the velocity magnitude and remains below the sensing area. Vertical velocity components are present only close to the instrument body and below the sensing area.

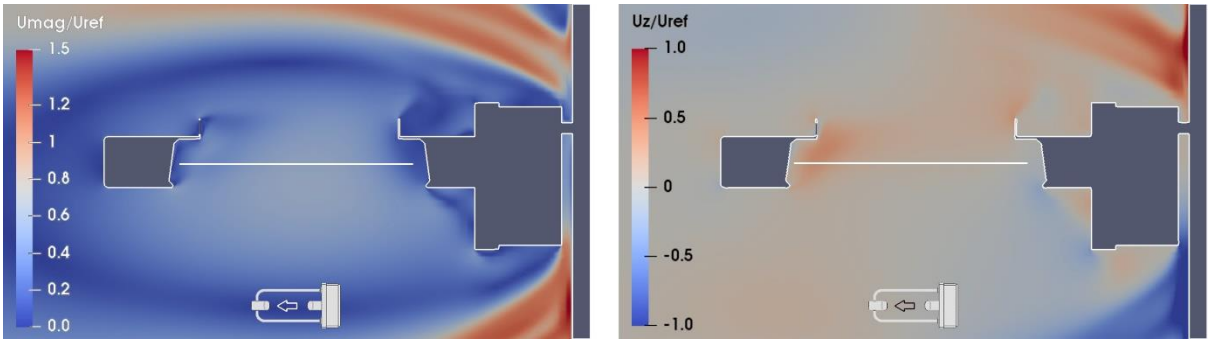

Figure 7: CFD simulation at 10 m/s and α = 180°; maps of the normalized magnitude and vertical component of the flow velocity (left- and right-hand panel, respectively). The white horizontal line indicates the position of the sensing area of the instrument, while the small arrow indicates the undisturbed flow direction.

In Figure 7, at α = 180° and wind speed 10m/s, the circuitry box and the supporting pole act as a relevant bluff-body obstacle for the flow generating a large recirculation zone completely enclosing the instrument body. Above the sensing area, two zones of first accelerated and then decelerated flow are present, with a considerable updraft.

The vortex structures near the instrument body are visualized in Figure 8 by means of the Q-criterion [17], while the turbulent kinetic energy is shown in Figure 9. At α = 0° (left-hand panel), the wake generated affect the sensing area of the instrument and the flow region above it. At α = 90° (central panel), neither the turbulence structures produced by the two heads and the circuity box, nor the turbulent wake produced by the supporting arm affect the sensing area of the instrument. At α = 180° (right-hand panel), the circuitry box produces large vortex structures that completely envelop the instrument sensing area.

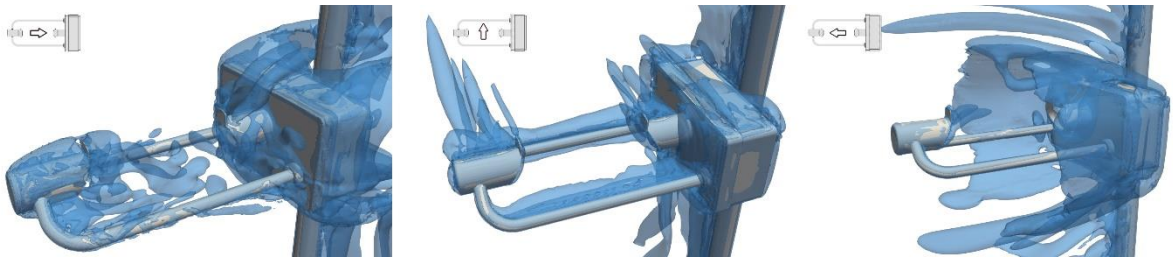

Figure 8: Visualization of the turbulent structures around the instrument using the Q-criterion at 10 m/s and α = 0°, 90°, and 180° in the left, central, and right-hand panels, respectively.

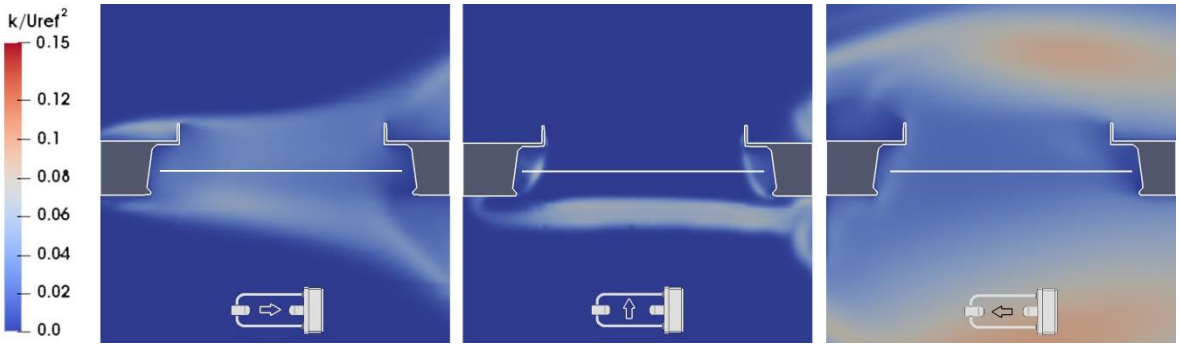

Figure 9: Maps of the normalized turbulent kinetic energy (k/Uref2) from CFD simulations at 10 m/s for α = 0°, 90°, and 180° in the left, central, and right-hand panels, respectively. The white horizontal line indicates the position of the sensing area of the instrument, while the small arrow indicates the undisturbed flow direction.

Similar results were obtained for other wind velocity and directions. Recirculation and vertical velocity components non-linearly decrease from the 0° configuration to the 90° configuration, where a minimum is reached, and then increase again approaching the 180° configuration, where the maximum amount of flow disturbance is obtained.

To compare the effect of wind between different instrument configurations, a control volume is defined, just above the sensing area, as a box with a length of 0.228 m, a height of 0.1 m and a width of 0.05 m. The long side of the box is along the laser beam, while the box lower face coincides with it. This volume represents the portion of the wind field having a strong potential to influence hydrometeors when approaching the instrument sensing area and provides an overall indication of the wind field deformation due to the presence of the instrument body. Maximum and average values of the vertical velocity components are reported in Table 1. It is confirmed that the lower impact is associated with the two configurations at 0° and 90° (and nearby angles). Maximum values are in

general higher when the wind impacts at an angle with respect to the instrument axis. The 22.5°, 45°, 135° and 157.5° configurations produce the highest values, because the flow is not blocked like in the 0° or 180° configurations, differently from angles close to 90° where the instrument presents the most favourable cross-section obstacle to the flow. In terms of average values and extension (percentage within the control volume), updraft is predominant (see the second-last column). The only two exceptions are the 135° and 157.5° configurations, where the circuitry box, with its large, slanted, bluff-body obstruction to the flow, produces predominant downdraft components in the control volume (see last column).

Wind direction	**Max updraft**	**Max downdraft**	**Avg. updraft**	**Avg. downdraft**	**% volume updraft**	**% volume downdraft**
0°	0.240	0.097	0.052	0.020	74.5	25.5
22.5°	0.629	0.386	0.095	0.052	79.3	20.7
45°	0.679	0.254	0.077	0.035	86.5	13.5
67.5°	0.410	0.150	0.057	0.022	91.3	8.7
90°	0.281	0.257	0.030	0.025	82.9	17.1
112.5°	0.553	0.158	0.041	0.030	92.9	7.1
135°	0.709	0.257	0.068	0.070	30.6	69.4
157.5°	0.649	0.410	0.068	0.159	3.2	96.8
180°	0.430	0.258	0.098	0.048	93.9	6.1

Table 1: Updraft and downdraft components within the control volume, obtained from CFD simulations as an average over the five wind speed values investigated.

b. WT measurements

Quality check of the WT measurements is necessary. First, the probe returns a null value in case of relevant airflow components reaching the probe from outside of a 45° acceptance cone; this is typical of recirculating flow and strong turbulence conditions. Second, the probe has a lower sensitivity of about 2 m/s, below which the measurement is deemed unreliable so as in case of turbulence intensity larger than 30%. The measurements were discarded in case null values exceeded 20% of the total sample or if outside the limits discussed above. The most critical configuration is at $\alpha = 180°$, where the combined effect of the circuitry box and the supporting pole produces strong recirculation zones and high turbulence intensity, with almost all measurements being rejected. On the other hand, the 67.5°, 90°, and 112.5° configurations, because of their favourable cross section obstacle presented to the incoming flow, are the least disturbed, with all measurements satisfying the quality, velocity, and turbulence intensity criteria.

c. Validation

Validation of the simulation results was performed by comparing the average simulated velocity with the measurements obtained in the WT experiment. In Figures 10, 11 and 12, simulated profiles and measured data are reported. For each value, error bars represent the measurement tolerance while the number reported quantifies the quality index. The simulations show a very good agreement with measurements for the three angles reported. Due to the large number of measurements taken, a statistical approach was used. For this analysis, only the 661 measurements satisfying the quality (>0.8), velocity (>2 m/s), and turbulence intensity (<0.3) criteria are considered. Only 44 out of the total

number of measurements considered (6.65%) differ from the simulation results by more than the instrument tolerance (equal to 0.5 m/s). The numerical simulation model is therefore capable of correctly capturing the phenomenon, especially for the more favourable configurations where the agreement is really good but providing satisfactory results even in the less favourable conditions of high turbulence and recirculating flow.

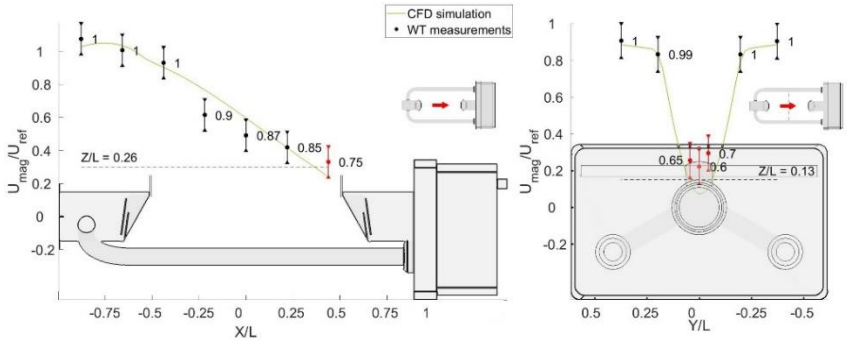

Figure 10: Comparison of the simulated profiles of the magnitude of flow velocity against WT measurements for the configuration at α = 0° and wind speed of 5 m/s.

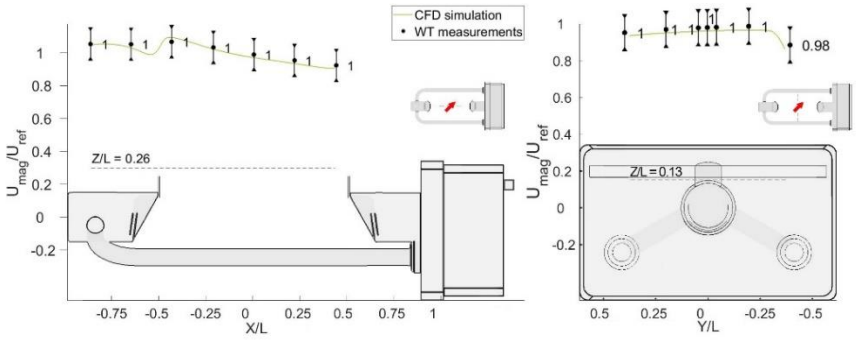

Figure 11: Comparison of the simulated profiles of the magnitude of flow velocity against WT measurements for the configuration at α = 45° and wind speed of 5 m/s.

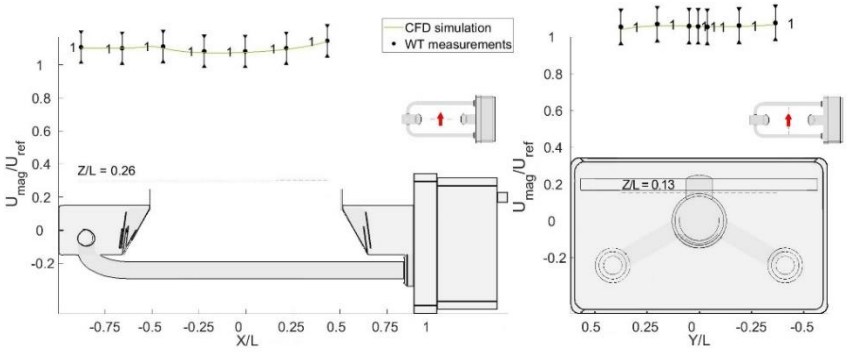

Figure 12: Comparison of the simulated profiles of the magnitude of flow velocity against WT measurements for the configuration at α = 90° and wind speed of 5 m/s.

d. Scalability

A scalability analysis was conducted to assess the validity of the solution at airflow velocities in between the simulated ones. Three further velocities (3, 7.5 and 15 m/s) were investigated to this end in the WT for three different wind directions (0°, 45° and 90°) and a few simulated wind velocity profiles above the instrument measuring area are illustrated

in Figure 13. For α = 45° and α = 90°, both the simulated profiles and measured data show almost no Reynolds number dependency, while for the 0° configuration some differences occur in areas with a high turbulence intensity.

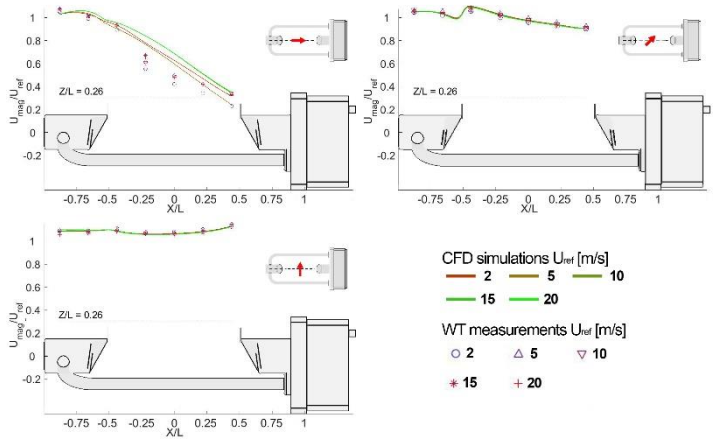

Figure 13: Reynolds number dependency of four simulated profiles for a wind speed of 2, 5, 10, 15, and 20 m/s normalised with the magnitude of the airflow velocity above the measuring area and WT measurements along the same profile at 3, 5, 7.5, and 15 m/s.

4. Conclusions

The aerodynamic behaviour of the complex outer geometry of NCGs induces vertical and accelerated/decelerated velocity components above and within the sensing area of the instrument. Both simulation results and WT measurements show that wind direction is the primary factor dictating the aerodynamic response of the Thies LPM, even more so than the wind speed, due to the demonstrably limited Reynolds number dependency. The airflow near the sensing area changes considerably and, in some cases, abruptly with the wind direction, showing a strongly non-linear behaviour that makes it difficult to predict the effect of wind without specific CFD simulations.

Near and above the sensing area, depending on the wind direction, the normalised average updraft is between 3% and 10% (with peak velocities up to 70% of the freestream value), while the normalised downdraft is between 2% and 16% (with peaks up to 40% of the freestream value). These strong velocity gradients near the instrument body are not negligible and potentially affect the approaching hydrometeors. These are indeed slowed down by strong updraft components or diverted away from the sensing area by strong transversal velocity components.

This should be considered when interpreting measurements obtained in windy conditions, because the observed airflow pattern generated by the gauge body is expected to induce non-negligible biases in operational measurements, especially in strong wind and light precipitation. The proposed airflow numerical simulation framework, that was suitably validated by means of wind tunnel experiments, provides a basis to develop correction curves for the wind-induced bias of NCGs, depending not only on the undisturbed wind speed and precipitation intensity, but also on the wind direction.

5. References

1. Lanza, L.G.; Merlone, A.; Cauteruccio, A.; Chinchella, E.; Stagnaro, M.; Dobre, M.; Garcia Izquierdo, M.C.; Nielsen, J.; Kjeldsen, H.; Roulet, Y.A.; et al. Calibration of non-catching precipitation measurement instruments: A review. *J. Meteorol. Appl.* **2021**, *28*, e2002, doi:10.1002/met.2002.
2. Sevruk, B. *Methods of Correction for Systematic Error in Point Precipitation Measurement for Operational Use*; Technical Report; WMO N. 589 OHR N. 21; World Meteorological Organization: Geneva, Switzerland, **1982**; ISBN 978-92-63-10589-9.
3. Cauteruccio, A.; Brambilla, E.; Stagnaro, M.; Lanza, L.G.; Rocchi, D. Experimental evidence of the wind-induced bias of precipitation gauges using Particle Image Velocimetry and particle tracking in the wind tunnel. *J. Hydrol*. **2021**, in press, doi:10.1016/j.jhydrol.2021.126690.
4. Colli, M.; Pollock, M.; Stagnaro, M.; Lanza, L.G.; Dutton, M.; O'Connell, P.E. A Computational Fluid-Dynamics assessment of the improved performance of aerodynamic raingauges. *Water Resour. Res.* **2018**, *54*, 779–796, doi:10.1002/2017WR020549.
5. Cauteruccio, A.; Lanza, L.G. Parameterization of the collection efficiency of a cylindrical catching-type rain gauge based on rainfall intensity. *Water* **2020**, *12*, 3431, doi:10.3390/w12123431.
6. Cauteruccio, A.; Chinchella, E.; Stagnaro, M.; Lanza, L.G. Snow particle collection efficiency and adjustment curves for the hotplate precipitation gauge *J. Hydrometeorol.* **2021**, *22*, 941–954, doi:10.1175/JHM-D-20-0149.1.
7. de Moraes Frasson, R.P.; Da Cunha, L.K.; Krajewski, W.F. Assessment of the Thies optical disdrometer performance. *Atmos. Res.* **2011**, *101*, 237–255, doi:10.1016/j.atmosres.2011.02.014.
8. Adirosi, E.; Roberto, N.; Montopoli, M.; Gorgucci, E.; Baldini, L. Influence of disdrometer type on weather radar algorithms from measured DSD: Application to Italian climatology. *Atmosphere* **2018**, *9*, 360, doi:10.3390/atmos9090360.
9. Bao, X.; Wu, L.; Zhang, S.; Yuan, H.; Wang, H. A Comparison of Convective Raindrop Size Distributions in the Eyewall and Spiral Rainbands of Typhoon Lekima (2019). *Geophys. Res. Lett.* **2020**, *47*, e2020GL090729, doi:10.1029/2020GL090729.
10. Iserloh, T.; Fister, W.; Seeger, M.; Willger, H.; Ries, J.B. A small portable rainfall simulator for reproducible experiments on soil erosion. *Soil Tillage Res.* **2012**, *124*, 131–137, doi:10.1016/j.still.2012.05.016.
11. Pickering, B.S.; Neely III, R.R.; Harrison, D. The Disdrometer Verification Network (DiVeN): A UK network of laser precipitation instruments. *Atmos. Meas. Tech.* **2019**, *12*, 5845–5861, doi:10.5194/amt-12-5845-2019.
12. Upton, G.; Brawn, D. An investigation of factors affecting the accuracy of Thies disdrometers. In Proceedings of the WMO Technical Conference on Instruments and Methods of Observation (TECO-2008), St. Petersburg, Russian Federation, 27–29 November **2008**; pp. 27–29.
13. Jeanmasson, G.; Mary, I.; Mieussens, L. On some explicit local time stepping finite volume schemes for CFD. *J. Comput. Phys.* **2019**, *397*, 108818, doi:10.1016/j.jcp.2019.07.017.
14. Pope, S.B. *Turbulent Flows*; Cambridge University Press: Cambridge, UK, **2000**; pp. 182–263.
15. Menter, F.R. Two-equation eddy-viscosity turbulence models for engineering applications. *AIAA J.* **1994**, *32*, 1598–1605, doi:10.2514/3.12149.
16. Turbulent Flow Instrumentation Pty Ltd. *Cobra Pressure Probe*; TFI Ltd.: Tallangatta, Victoria, Australia: **2011**.
17. JCR, H.; Wray, A.; Moin, P. *Eddies, Stream, and Convergence Zones in Turbulent Flows*; Center for Turbulence Research Report CTR-S88; Stanford University: Stanford, CA, USA, **1988**; pp. 193–208.